Precise spectral directional infrared emissivity of a Cantor high-entropy alloy

Cite as: AIP Advances 14, 075211 (2024); doi: 10.1063/5.0206928
Submitted: 17 March 2024 • Accepted: 1 July 2024 •
Published Online: 11 July 2024

Jon Gabirondo-López,[1,a] Iñaki López-Ferreño,[2] Boris Straumal,[3,b] Alena Gornakova,[3,c] Anna Korneva,[4,d] Olga Kogtenkova,[3,e] Telmo Echániz,[5,f] and Gabriel A. Lopez[1,g]

AFFILIATIONS

[1] Physics Department, University of the Basque Country (UPV/EHU), Leioa, Spain
[2] Applied Mathematics, University of the Basque Country (UPV/EHU), Vitoria-Gasteiz, Spain
[3] Osipyan Institute of Solid State Physics of the Russian Academy of Sciences, Ac. Osipyan str. 2, 142432 Chernogolovka, Russia
[4] Institute of Metallurgy and Materials Science, Polish Academy of Sciences, Reymonta St. 25, 30-059 Cracow, Poland
[5] Applied Mathematics, University of the Basque Country (UPV/EHU), Bilbao, Spain

[a] jon.gabirondol@ehu.eus
[b] **Author to whom correspondence should be addressed:** straumal@issp.ac.ru.
Tel.: +7 916 6768673. **Web:** www.issp.ac.ru/libm/staff
[c] alenahas@issp.ac.ru
[d] annakor108@gmail.com
[e] kogtenkova@issp.ac.ru
[f] telmo.echaniz@ehu.eus
[g] gabrielalejandro.lopez@ehu.eus

ABSTRACT

The multicomponent equiatomic CrMnFeCoNi alloy was proposed by B. Cantor almost 20 years ago and was the first in the family of the so-called multiprincipal or high-entropy alloys (HEAs). Various mechanical properties of the Cantor alloy and its derivatives, such as corrosion behavior, oxidation resistance, irradiation response, diffusion bonding, and weldability, have been studied these past years. Unfortunately, data on their thermo-physical properties are scarce and the information about infrared emissivity is completely absent. Having reliable infrared emissivity data at working conditions is very important for non-contact temperature measurements and for modeling heat transfer by radiation during manufacturing. In this work, a Cantor alloy, as a typical example of HEAs, was manufactured with levitation melting in vacuum. The alloy contains mainly one phase with face-centered cubic lattice and small amount of oxide precipitates. The angle-dependent spectral directional emissivity was measured between 200 and 700 °C. Reproducible data were obtained upon several thermal cycles. The total directional emissivity is almost constant from 10° to 50°, and it increases up until it reaches a maximum around 70°. Integrating these data, total hemispherical emissivity was determined, and it was observed that this property remains almost constant at 0.28 in a wide temperature range, showing a minor increase with increasing temperature. Spectral directional emissivity measurements allow detecting incipient oxidation processes. These data show the necessity of measuring emissivity at working temperatures to achieve a precise quantification of radiative heat transfer.

I. INTRODUCTION

High entropy alloys (HEAs) build a class of metallic materials characterized by the presence of multiple principal elements in roughly equal or near-equal atomic proportions. These alloys are known for their unique properties stemming from their complex, multicomponent composition. Multicomponent alloys with five and more components without principal one (called also HEAs) were first proposed by Cantor *et al.*[1] and Yeh *et al.*[2] It was astonishing that the alloys consisting of so many elements can build the uniform face-centered cubic (fcc) solid solution. Since its discovery, the five-component equiatomic CrMnFeCoNi alloy is called Cantor

alloy and is one of the most-studied HEAs. From the very beginning, the unique mechanical properties of HEAs were expected, and, therefore, they are the most investigated for Cantor alloy and its derivatives. The tensile properties,[3–11] nanoindentation,[12–15] fatigue properties,[16–20] hardness,[14,21–24] compressive strength,[21,25–27] high strain rate and spall behavior (shock response),[28] ballistic impact,[29] fracture mechanisms,[5,30] creep,[31] torsion at high strains and temperatures,[32] wear,[33] mechanisms of plastic deformation,[34–36] strain hardening,[37] and thermal expansion[38] were studied in detail. Meanwhile, the corrosion behavior,[3,39–41] oxidation resistance,[15,42–44] irradiation response,[45] diffusion bonding,[46] and weldability[47] were also studied in the past. Much less attention was devoted to other physical properties of Cantor alloys, such as magnetic properties,[48–53] thermoelectric performance,[54] photoemission,[55] and ability to build supercapacitors.[56] Together with the ideal equiatomic CrMnFeCoNi alloy, many Cantor-based alloys with Al,[3,44,57–59] Zr,[60] Ti,[61,62] Si,[61] Fe,[63,64] Nb,[22] Ni,[65] Cu,[44] nitrogen,[5,9,21,66,67] and carbon[10,22,43] additions were proposed and investigated looking forward to improving particular properties.

However, less attention was devoted to radiative properties, i.e., infrared emissivity, of Cantor alloys and generally of HEAs. A lack of reliable data on that issue in the literature is manifest. Spectral directional emissivity studies are the most versatile tool to investigate these properties. Compared to other methods, direct radiometric techniques are more sensible because they collect the spectral information that can vary with the surface conditions, temperature, emission angles, etc. Such studies have been previously performed for metallic alloys designed for aeronautics,[68,69] fusion reactors,[70] or machine tooling.[71] In general, knowledge on infrared emissivity is of utmost importance in alloys and intermetallics for a several reasons. First, spectral directional emissivity values are needed to measure temperatures via non-destructive testing (NDT) techniques, such as pyrometry or thermography, as good non-contact temperature measurements via pyrometers and/or thermographic cameras need precise emissivity values at certain wavelengths or wavelength range. In addition, angle-dependent measurements are often necessary, as measuring devices cannot always point at a sample at normal or near-normal angles. Such measurements are widely performed during casting or laser metal deposition (LMD) to monitor/control the synthesis processes.[72] Moreover, total hemispherical emissivity, a parameter that can be determined by integrating spectral directional emissivity data, is needed to model metal deposition heat transfer of additive manufacturing processes.[73] Furthermore, total hemispherical emissivity is used to account for heat radiation losses and is needed to understand heat transfer mechanisms in hydrogen storage technologies.[74] Finally, the spectral emissivity measurements have proven to be an effective method to study surface oxidation kinetics *in situ*.[75] According to this background, consistent and accurate emissivity measurements are of great importance for the scientific community from several points of view.

In this work, a Cantor alloy, as a typical example of HEAs, was manufactured and its radiative properties were explored systematically: the synthetized sample was exposed to several thermal treatments, while its spectral directional emissivity was measured *in situ*. Those annealing-like thermal treatments were performed in the range of typical working temperatures, from room temperature up to 900 °C. After each cycle, the microstructure and composition of the sample was studied. Finally, the data obtained through those spectral directional experiments were integrated to obtain the total directional and total hemispherical emissivity values. Thus, the novel characterization presented in this work can serve to develop and implement scientific and industrial solutions based in these alloys.

II. EXPERIMENTAL PROCEDURE

A. Sample preparation

The high-entropy alloy CrMnFeCoNi, consisting of 19.37 wt. % Cr, 18.92 wt. % Mn, 19.51 wt. % Fe, 20.77 wt. % Co, and 21.16 wt. % Ni, was prepared by the levitation melting of pure metals in vacuum. Pure metals have been used, such as chromium (99.99 wt. %), manganese (99.99 wt. %), iron (99.99 wt. %), cobalt (99.98 wt. %), and nickel (99.98 wt. %), to produce the alloy. Then, the material was cast into a cylindrical ingot with a diameter of 20 mm (Fig. 1). The ingot was cut into 2 mm thick disks using spark erosion Electroerosive Wire Machine with NPC System (Model: DK7735, China). The surface-hardened layer was removed using the grinding paper with the roughness of 68 μm. Then, the sample was mechanically polished with a diamond paste of particle size down to 1 μm and, finally, with an alumina suspension of 0.05 μm particle size.

B. Infrared emissivity measurements

The directional spectral emissivity of a surface is the thermophysical property that quantifies its capacity to emit thermal radiation at a temperature T, a wavelength λ, and an emission direction defined by the polar and azimuthal angles θ and φ. Formally, it is defined as

$$\varepsilon(T,\lambda,\theta,\varphi) = \frac{L_{surface}(T,\lambda,\theta,\varphi)}{L_{blackbody}(T,\lambda)}, \quad (1)$$

where $L_{surface}$ and $L_{blackbody}$ are, respectively, the radiance emitted by the studied surface and the spectral radiance emitted using a perfect emitter that follows the Planck radiation law: a blackbody.

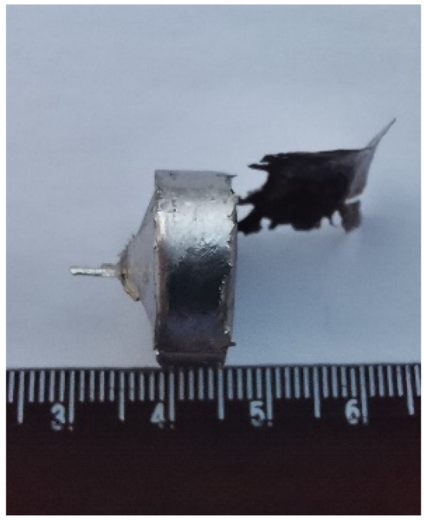

FIG. 1. The as-cast sample of CrMnFeCoNi alloy.

For the cases in which the surface does not have any dependence with the azimuthal angle, the spectral emissivity can be integrated over the spectral axis in order to obtain the total directional emissivity,

$$\varepsilon_T(T,\theta) = \frac{\int_0^\infty \varepsilon_T(T,\lambda,\theta) L_{blackbody}(T,\lambda) d\lambda}{\int_0^\infty L_{blackbody}(T,\lambda) d\lambda}. \quad (2)$$

Finally, total hemispherical emissivities can also be calculated by integrating over the entire solid angle,

$$\varepsilon_H(T) = \int_0^{\pi/2} \varepsilon_T(T,\theta) \sin(2\theta) d\theta. \quad (3)$$

At temperatures between room temperature and 1000 °C, most of the radiation emitted by a surface is found in the mid-infrared range, i.e., more than 95% of the radiation is enclosed in this range. Thus, performing infrared emissivity measurements at working temperatures for various emission angles allows estimating correctly the total hemispherical emissivity of a surface.

The HAIRL emissometer was used to measure the spectral infrared emissivity of the sample. The emissometer was built from original designs,[76] and it consists of a Fourier-transform infrared spectrometer (FTIR), a vacuum sample chamber, a reference blackbody (Isotech Pegasus 970 R®), and an optical entrance box placed in a T-form geometrical configuration. The spectrometer is a Bruker Vertex 80v model. Its optical system consists of conventional KBr optics, a Ge/KBr beam splitter, and a DLaTGS detector. Thus, emissivity experiments can be performed in a maximum range of 1.43–25 μm. As explained in Gonzalez de Arrieta *et al.*,[77] two type K thermocouples are welded near the measuring spot in order to measure the emissivity of metallic samples. Those thermocouples are used to control the temperature of the sample and to calculate its spectral emissivity. Consequently, the temperatures measured during the emissivity experiments also allow us to register the thermal history of the sample in a reliable manner.

C. Microstructural characterization techniques

Jeol JSM 6400/7000F scanning electron microscopes equipped with Oxford Instruments LINK ISIS energy dispersive x-ray spectrometers (EDS) were employed for the microstructure characterization and elemental analysis. X-ray diffraction (XRD) patterns were collected with the aid of the XPert-Pro diffractometer (manufactured by L Malvern PANalytical, Spectris Plc, Malvern, UK) using Cu K_α radiation in Bragg–Brentano geometry with an angular step size of 0.02° in order to perform structural-phase analysis of the samples. PowderCell 2.4 program (PowderCell for Windows, version 2.4. 03/08/2000, Werner Kraus, and Gert Nolze, BAM, Berlin, Germany) was utilized for phase analysis and calculation of lattice parameters. Texture evaluation of the sample was measured using a Bruker D8 Discover diffractometer (Bruker, Billerica, MA, USA) equipped with a Cr Twist tube, a V filter (λ = 2.2910 Å), a PolyCap™ (1 μm single crystal cylinders) system for parallel beam generation (divergence of 0.25°), and a 1D LynxEye detector (active length in 2θ 2.6°). The sample was mounted on an Eulerian Cradle with an automatically controlled X–Y–Z stage. Data were collected for the three most intense peaks reflections, using a fixed mode and time per orientation of 5 s. The data collection in thinned mode with 5° of δ was measured for full circle 0–360 incr. 5° in phi (φ) and 0–70 incr. 5° in psi (ψ) range, giving 2079 total orientations.

D. Stages along the whole investigation

In this subsection, all steps experienced by the sample along the whole investigation will be briefly described to provide the readers with the complete experimental history. First, the microstructure of the as-received sample was analyzed before starting the emissivity measurements. Afterward, the sample was attached to the sample holder of the emissometer and inserted into the vacuum chamber. The chamber was evacuated at room temperature. Once the vacuum level was below 4×10^{-4} mbar, the spectral directional emissivity measurements were performed from 100 to 400 °C every 100 °C, and at each temperature, the emission angle was changed from 10° to 80° using 10° steps. During those emissivity measurements, the sample was heated with a heating rate of about 100 °C per hour, and the sample was maintained at each temperature setpoint for about another hour to recollect the infrared radiation for the set of selected emission angles. The thermal history of those measurements is shown in Fig. 2.

Subsequently, after that first annealing-like treatment applied to acquire emissivity data up to 400 °C, the sample was cooled down to room temperature and again a microstructural characterization was performed. This first *in situ* thermal treatment was applied with the purpose of homogenizing the sample and carefully checking if there was a potential precipitation of secondary phases, and at the same time recording information on the emissivity.

Having observed no evidences of oxidation after the first set of measurements, a second emissivity experiment was performed every 100 °C from 100 °C up to a higher temperature of 700 °C for the same set of emission angles. After cooling down the sample, it was possible for naked eyes to observe a very slight surface oxidation, which could also be deduced by looking at the emissivity spectra and was confirmed by microstructural characterization. Afterward, the sample was polished again with an alumina suspension of 0.05 μm particle size in order to remove the thin oxide layer formed during the emissivity experiment. Then, the sample was measured again following the procedure explained before but in this run with a maximum temperature of 900 °C.

Finally, after the third run of measurements, the sample was polished again analogously and its spectral directional emissivity

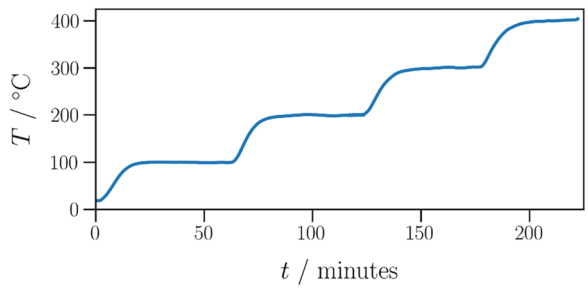

FIG. 2. Temperature profile acquired during the first set of emissivity measurements.

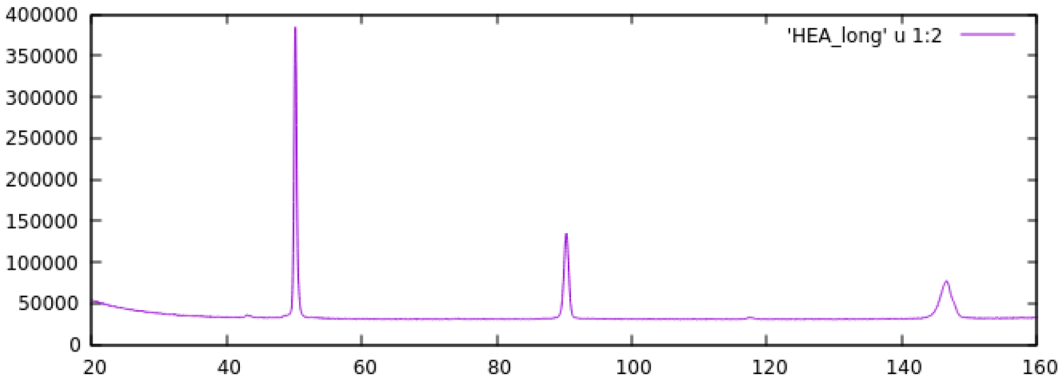

FIG. 3. XRD pattern of the CrMnFeCoNi HEA sample at room temperature.

was measured from 200 °C up to 800 °C every 100 °C, obtaining reproducible data for each temperature. Measurements acquired at 100 °C were skipped because the signal to noise ratio was too low in most of the spectral range. To avoid redundancy, emissivity data corresponding only to the last set of emissivity measurements will be presented in this contribution, because all important conclusions concerning the radiative behavior of the Cantor HEA can be addressed from them. In other words, thermal cycling was applied to confirm the microstructural stability of the HEA, while at the same time checking that the emissivity does not change upon cycling.

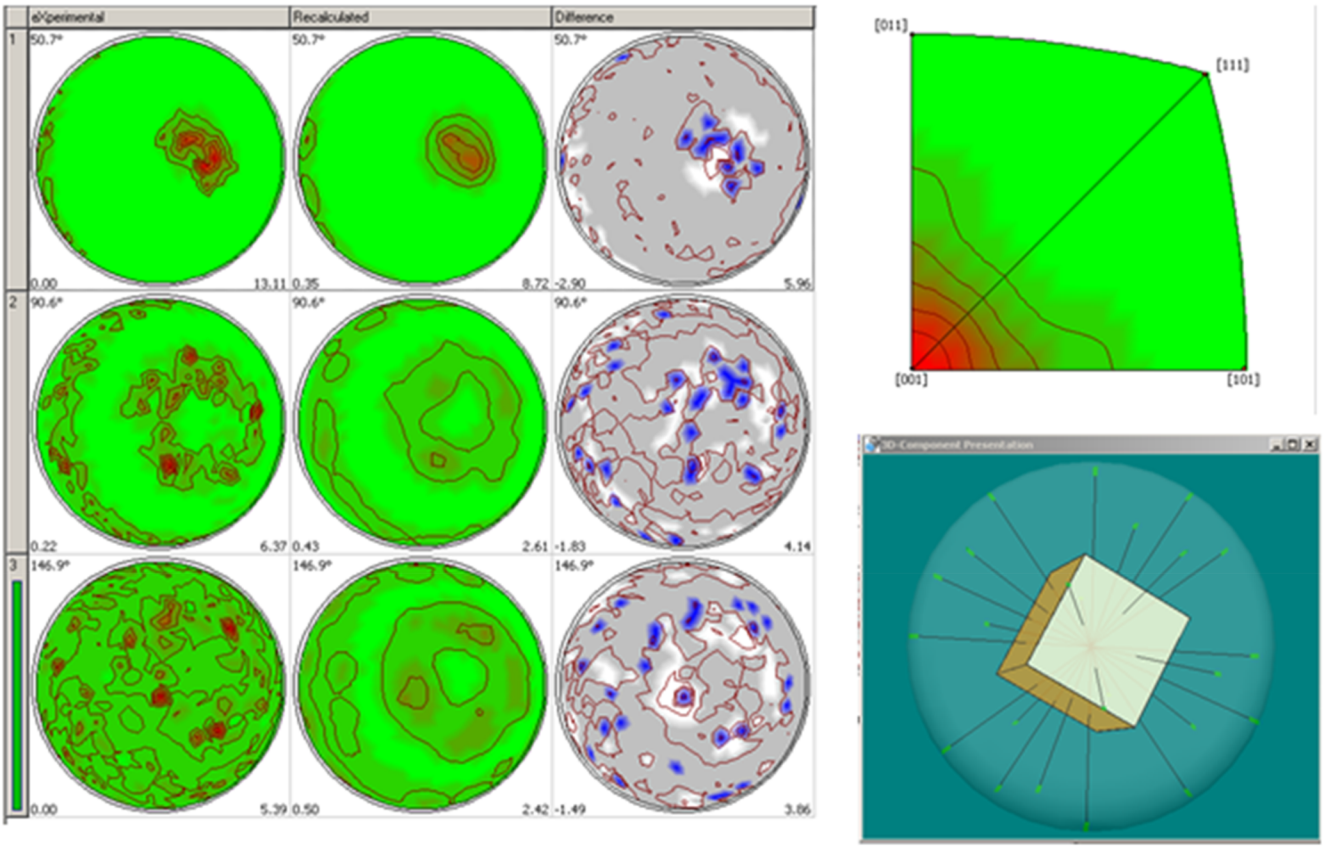

FIG. 4. Texture analysis: pole figure and preferential crystallographic orientation [100].

III. RESULTS AND DISCUSSION

A. Starting microstructural characterization before infrared emissivity measurements

Before investigating the emissivity of the Cantor HEA, the microstructure of the as-received sample was analyzed. Figure 3 shows the XRD pattern of the CrMnFeCoNi HEA sample measured at room temperature in the as-received state. All peaks belong to the same fcc phase with a lattice parameter a = 0.3596 nm. The distribution of peak intensities reveals a significant texture. The texture of the sample has been studied following the evolution of the three most intense peaks corresponding to the (200), (311), and (420) reflection at 50, 90, and 147° in 2θ, for different sample inclinations (see Fig. 4). The texture analysis confirms that ~50% of the volume corresponds to crystals with an orientation close to the [100] direction. In addition, the SEM backscattered electron (BSE) images (Fig. 5) reveal an acicular microstructure of the fcc main phase, in which the presence of two different precipitate phases can be observed. On the one hand, globular shape precipitates (bright particles) were observed in a small amount, and on the other hand, coherent or semi-coherent precipitates (dark particles) appear in the neighborhood (see Fig. 5). In addition, a dendritic-like structure with perpendicular branches can be identified at higher magnifications.

In order to complete the characterization, the composition of the precipitates and the acicular microstructure have been studied via EDS (Fig. 6). The globular bright precipitates have a remarkable Hf content (heavy element) and also a significant O content. Very probably, these precipitates are Hf oxides coming from the oxidation of Hf impurities during the melting of the alloy. In the case of the coherent dark precipitates, the EDS maps (Fig. 6) indicate a slightly higher Mn content in comparison with the other metals, which seem to indicate that they are Mn-rich oxides. Ti is present in these Mn rich precipitates, which contrasts with the rest of the regions where it is not observed.

B. Microstructural characterization after the first run of infrared emissivity measurements up to 400 °C

After the first set of emissivity measurements up to 400 °C, no oxidation is observed and the Hf-rich globular bright oxides and the coherent dark precipitates exhibit a similar size as those observed in the as-received state (Fig. 7). In addition, a similar acicular microstructure is present. However, the perpendicular branches of the dendritic-like microstructure are not observed. Texture analysis (Fig. 8) reveals that ~10% of the volume corresponds to crystals with an orientation close to the [100] direction, which indicates that the sample undergoes a texture evolution during the annealing-like treatment applied in the emissivity experiment performed up to 400 °C. The absence of the dendritic like structure suggests that the evolution of the texture is related to the disappearance of this structure.

C. Microstructural characterization after the second run of infrared emissivity measurements up to 700 °C

After the measurements up to 700 °C, a minor oxidation is observed on the surface of the HEA sample (Fig. 9), although the measurements were done under vacuum. This slight oxidation takes place in the whole surface, but it is significantly more remarkable at the grain boundaries, which are decorated with oxide particles. It is well-known that grain boundaries are preferable nucleation sites due to their higher energy in comparison with the bulk (also higher diffusivities). Finally, the oxide layer was removed and the sample was polished before the next set of emissivity measurements. At this stage, the microstructure was checked and the obtained backscattered electron image (Fig. 10) revealed a distribution of the Hf-rich bright oxides and Mn-rich dark precipitates similar to that observed in the sample emissivity experiment performed up to 400 °C. Therefore, it can be said that the microstructure of the bulk remains without significant changes.

D. Microstructural characterization after the third run of infrared emissivity measurements up to 900 °C

In this case, as expected from the observed emissivity spectra, there is a significantly stronger oxidation in the entire surface in comparison with the slight oxidation observed after the emissivity experiment performed up to 700 °C. Figure 11 shows the appearance of the surface of the Cantor HEA after the third run of emissivity measurements acquired up to 900 °C. The grain boundaries continue leading the oxide formation, but the oxidation in the bulk of the grains is clearly stronger.

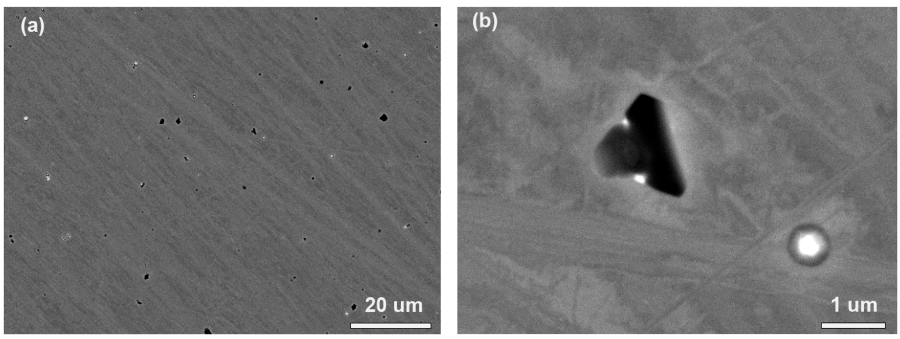

FIG. 5. BSE images of the studied HEA sample at different magnifications. (a) Overall microstructure of the fcc main phase of the HEA. (b) Globular shape precipitates (bright particles) and coherent or semi-coherent precipitates (dark particles) were observed in a small amount.

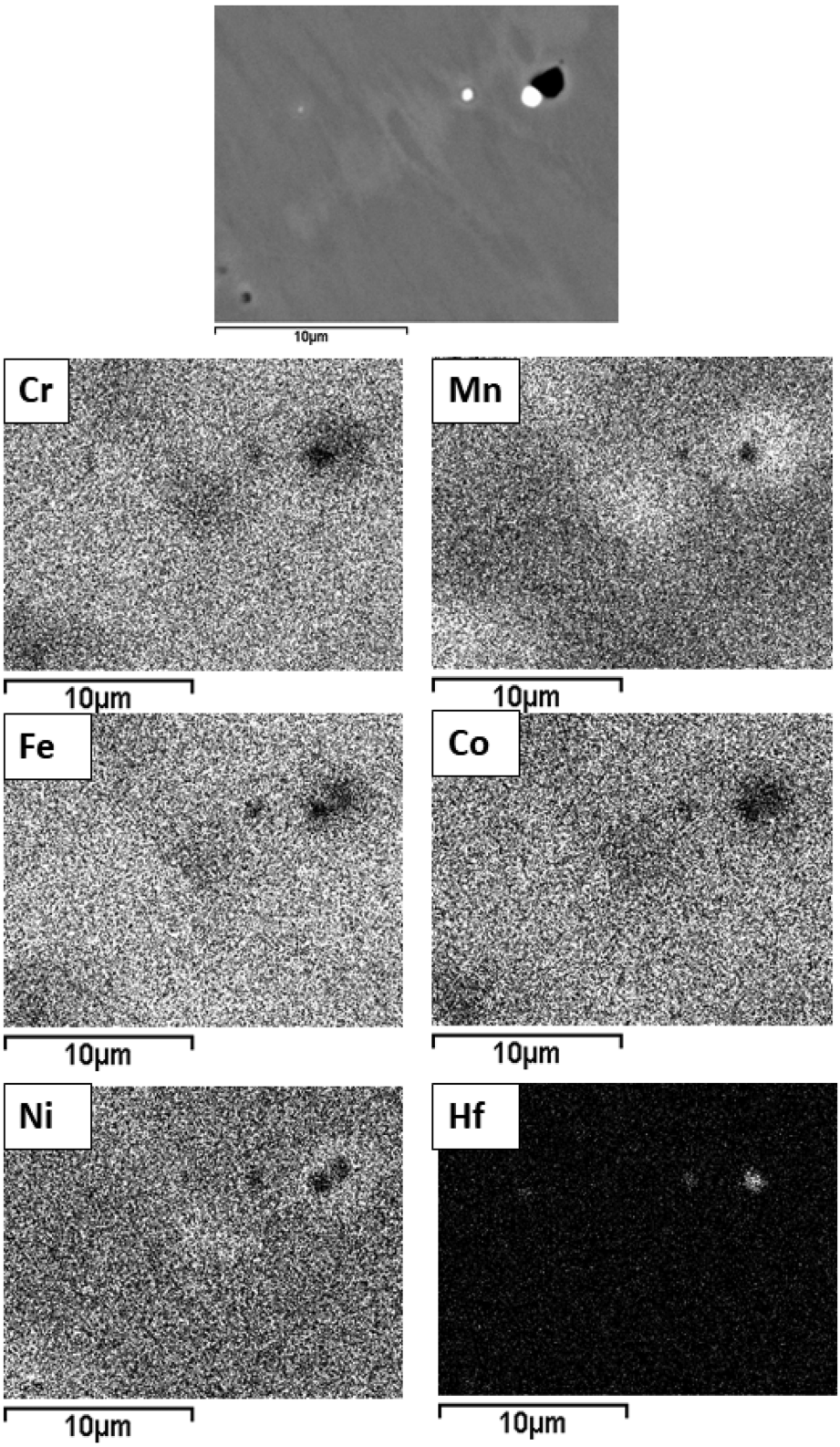

FIG. 6. Compositional EDS maps of a region of the sample with the two kinds of precipitates.

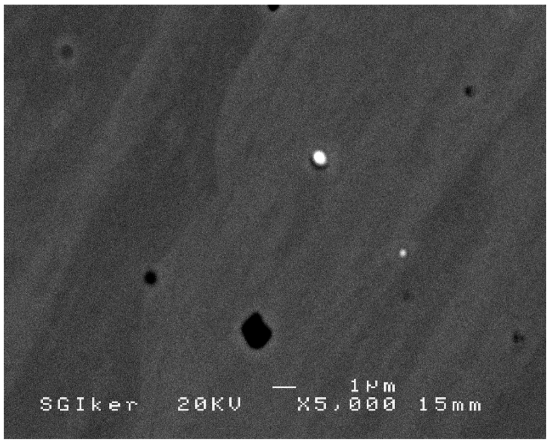

FIG. 7. BSE image of the HEA sample after emissivity measurements acquired up to 400 °C.

E. Infrared emissivity measurements

Several emissivity measurements were performed with the same sample. No significant difference between the spectral emissivity measurements was obtained at the same temperature in each experiment. Consequently, as mentioned above, only the data obtained for the last experiment are reported and used to estimate the total directional and total hemispherical emissivities. The exact methodology used to compute the value and the uncertainties of the integrated emissivities is explained in detail in Ref. 77.

For temperatures between 200 and 600 °C, the spectral emissivity values correspond to those of a metallic sample, as it is shown in the left column of Fig. 12. The spectral emissivity decreases monotonically with increasing wavelength. Its total directional emissivity remains constant for small emission angles and then increases at higher angles until it reaches a maximum around 70°. This behavior is coherent with the electromagnetic theory.[78]

For the experiments performed at 700 and 800 °C (see Fig. 13), an absorption band corresponding to a superficial oxide layer formed during the experiment can be seen first in the spectral emissivity recorded with a viewing angle of 50° at 700 °C and then between 40° and 80° at 800 °C. The measurements done at the latter temperature also show an increase in the emissivity at short wavelengths, also evidencing an incipient unavoidable oxidation for the vacuum level of the used setup. Taking that into account, it can be said that the spectra obtained at these high temperatures do not correspond entirely to the radiative behavior of the alloy, but that there is a contribution of a semitransparent thin oxide layer. Consequently, the emissivity measurements performed at higher temperatures will show the apparent emittance. Due to this reason, emissivity data acquired at 900 °C are not included, as the study

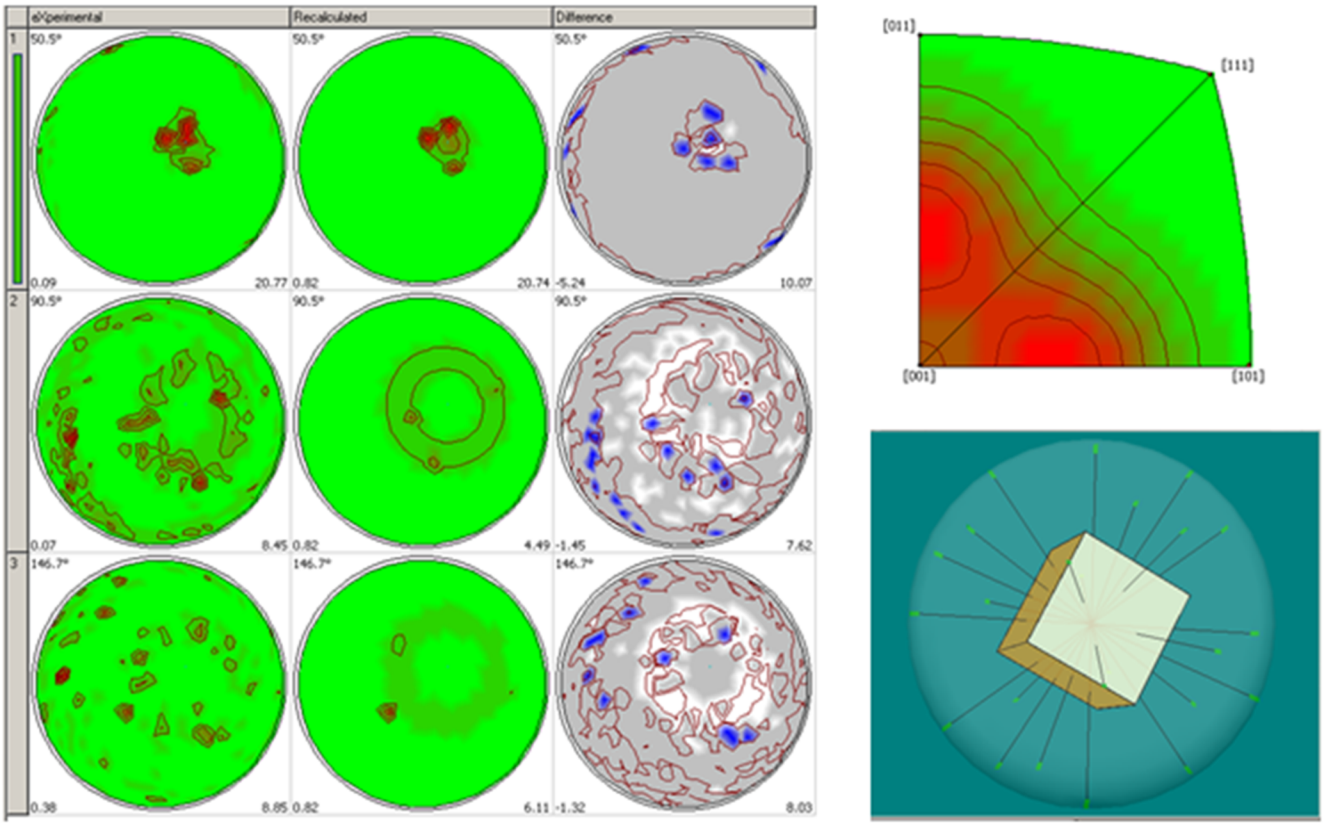

FIG. 8. Texture analysis: pole figure and preferential crystallographic orientation [100] after emissivity measurements acquired up to 400 °C.

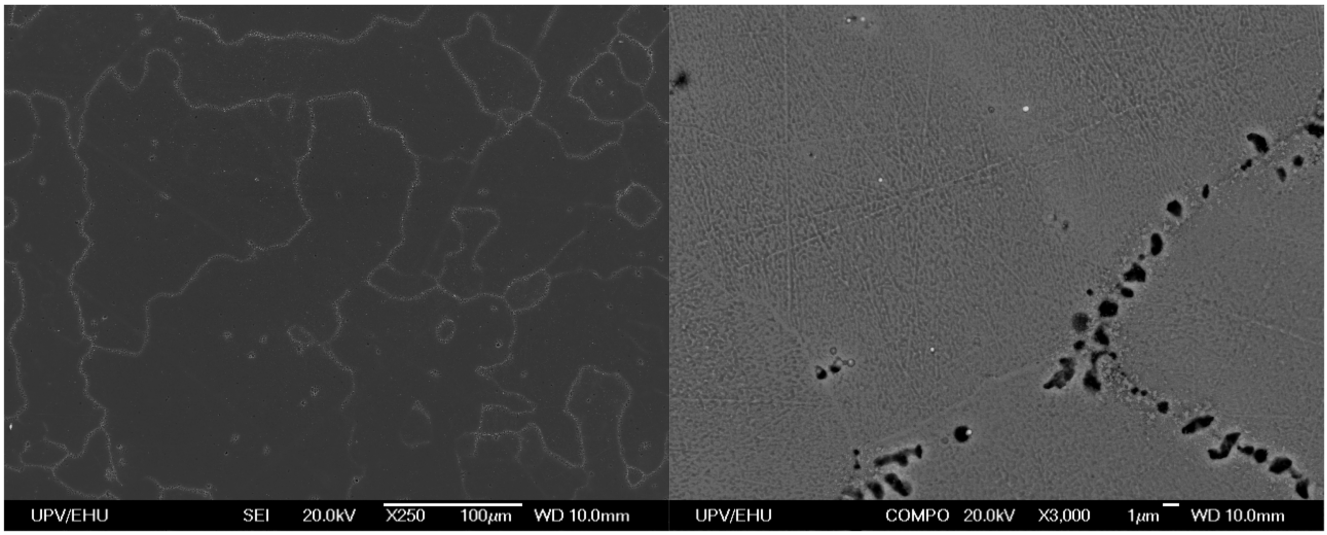

FIG. 9. Secondary and backscattered electron images at different magnifications of the surface of the Cantor HEA after emissivity measurements acquired up to 700 °C.

of the oxidation kinetics of the alloy is out of the scope of this work.

Considering all the collected emissivity spectra, we can state that the spectral emissivity of the studied alloy increases slightly with increasing temperature in the range from 200 to 600 °C, as it is shown in Fig. 14 (for the sake of simplicity, only data corresponding to three temperatures are shown). Moreover, for wavelengths longer than 5 μm, the differences of the spectral emissivities obtained at the near-normal emission angle are almost negligible up to 600 °C. The near-normal spectral emissivity measured at 800 °C shows a considerable increase for all recorded wavelengths. The measurements done at an emission angle of 50° show a small absorption peak at 15 μm, which is not noticeable for smaller angles. The oxide layer formed during the experiments also significantly affects the total hemispherical emissivity, as it is shown in Fig. 15. At temperatures below 700 °C, the total hemispherical emissivity shows a slight increase with increasing temperature, and this tendency changes abruptly when surpassing that threshold.

Finally, spectral emissivity data are compared to data from the literature. Although no emissivity data for HEAs are available, it is

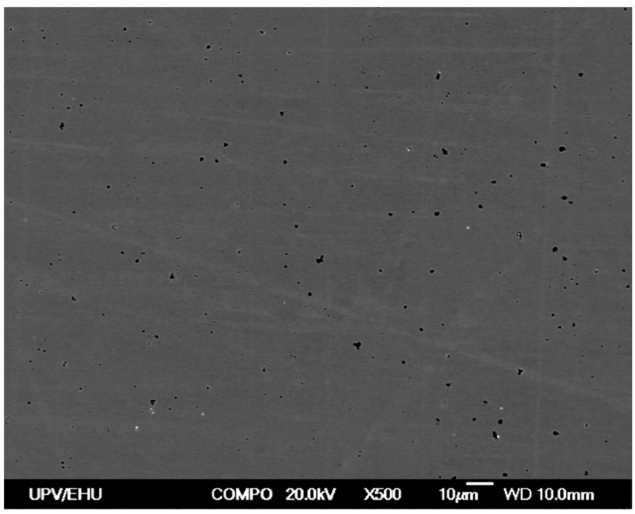

FIG. 10. Backscattered electron images of the bulk of the Cantor HEA after emissivity measurements acquired up to 700 °C and ulterior polishing.

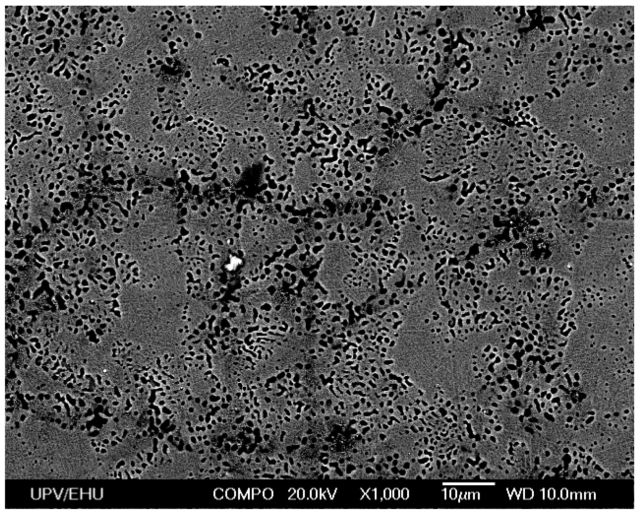

FIG. 11. Backscattered electron image of the surface of HEA sample after emissivity measurements acquired up to 900 °C.

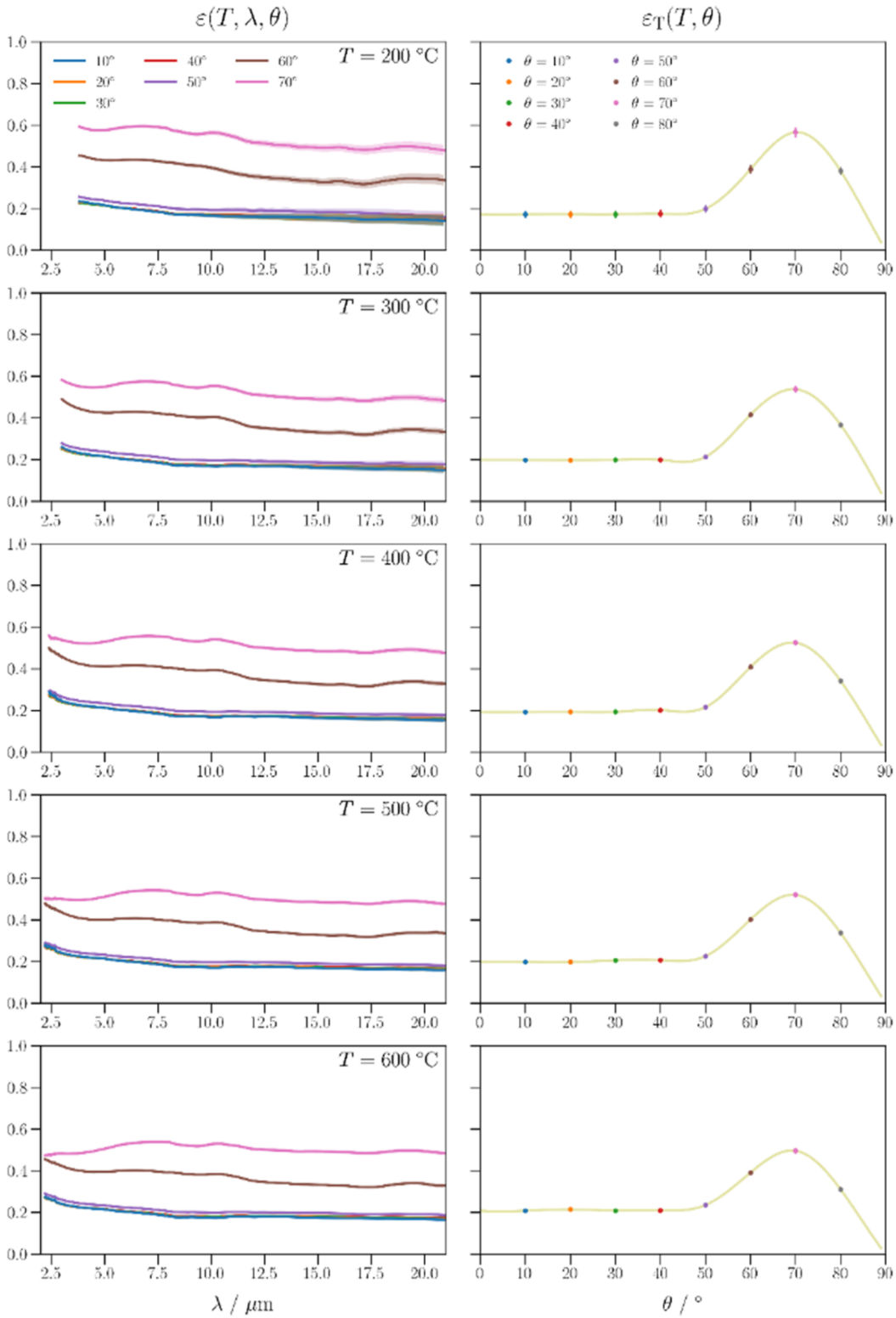

FIG. 12. Left: spectral directional emissivity acquired at temperatures between 200 and 600 °C. Right: total directional emissivity and its expanded uncertainty ($k = 2$) as a function of emission angle at the corresponding temperatures.

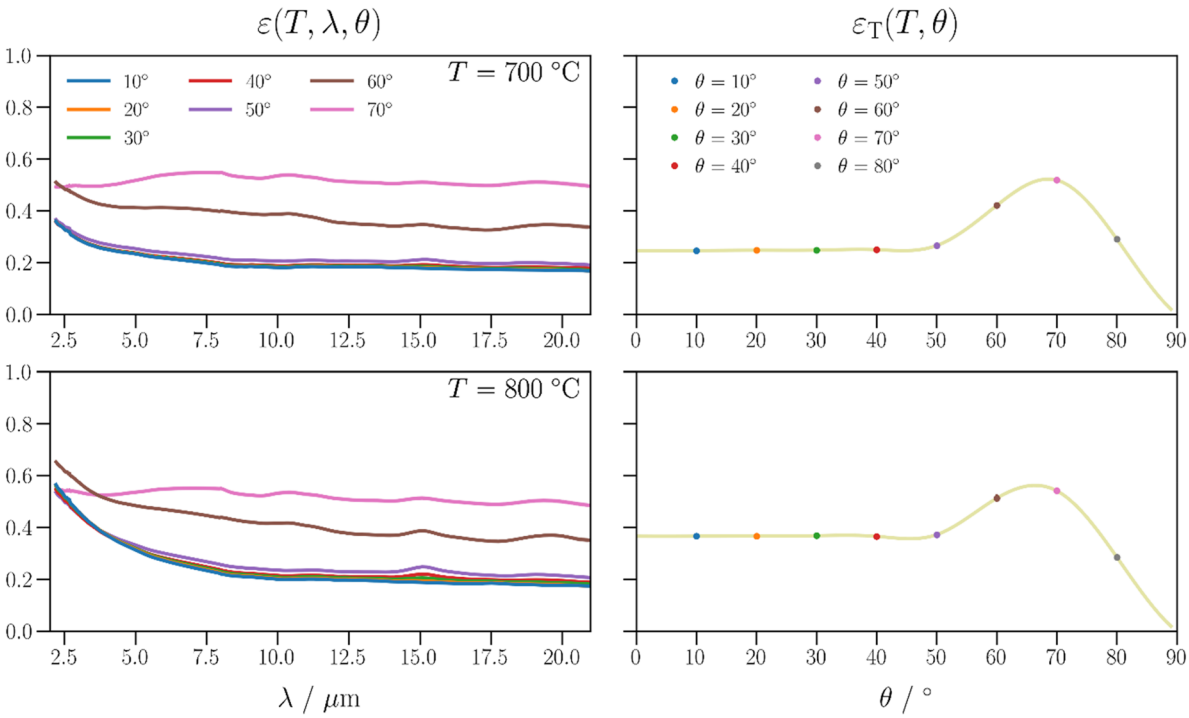

FIG. 13. Left: spectral directional emissivity acquired at temperatures between 200 and 600 °C. Right: total directional emissivity and its expanded uncertainty (k = 2) as a function of emission angle at the corresponding temperatures.

of interest to qualitatively compare the data of emissivity measurements for other metallic materials. In Fig. 16, near-normal emissivity data at 500 °C are compared to two sets of data from alloys used in the aerospace industry: first, data at 527 °C from an Inconel 718 (nickel-based) alloy are plotted in orange.[68] In addition, analogous data published for a Ti–6Al–4V alloy at 441 °C are shown in green.[79] Data corresponding to pure Ni at 493 °C are also provided in this figure as a reference of a pure metal.[77] First of all, it is worth mentioning that the emissivity values acquired for the Cantor HEA are in the order of magnitude observed for metallic materials. However, although for short wavelengths (λ < 7 μm), the typical monotonic decrease with increasing wavelengths is observed, for longer

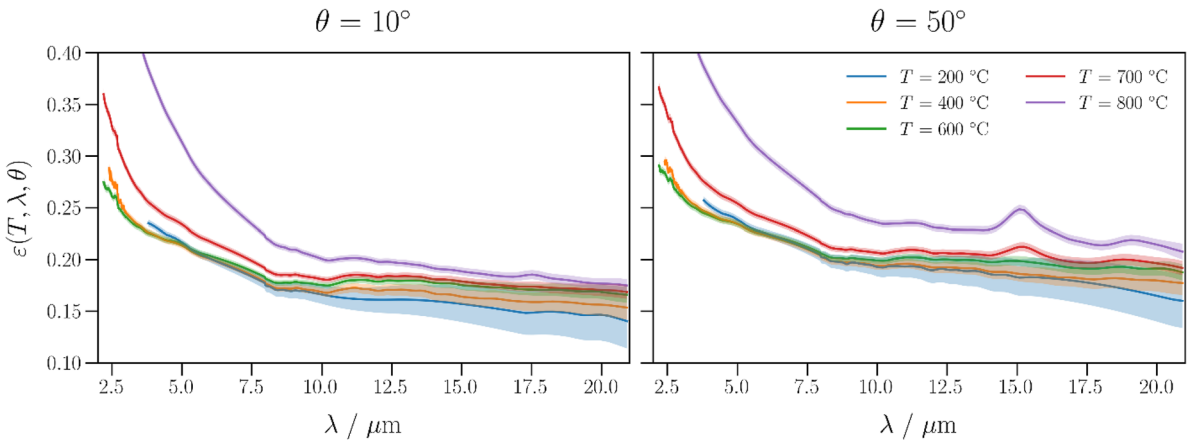

FIG. 14. Spectral directional emissivity for two emission angles at three temperatures before the oxidation started (T = 200, 400, and 600 °C) and at two temperatures after a thin oxide layer began to grow on the surface (T = 700 and 800 °C).

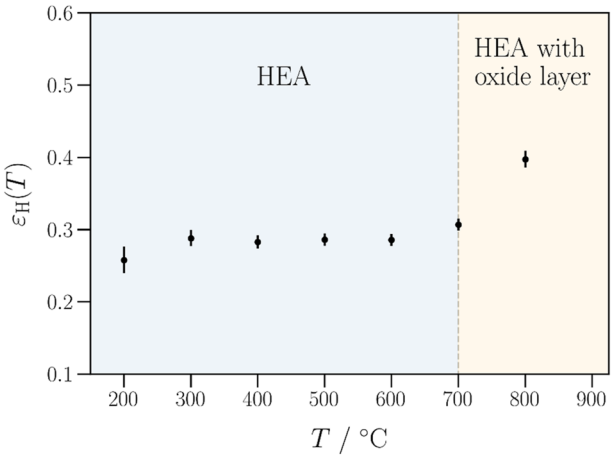

FIG. 15. Total hemispherical emissivity from T = 200 °C to T = 800 °C with their expanded uncertainties (k = 2). The measurements corresponding to the alloy are shaded in blue, and the measurements corresponding to the alloy with the thin oxide layer are shaded in orange.

wavelengths, the emissivity of the studied Cantor HEA remains quite constant (in contrast to the parallel tendency observed for the other three metallic materials). In particular, for wavelengths beyond 15 μm, it can be said that the emissivity level is relatively high. A reasonable explanation for such a behavior can be provided if we consider the large electron scattering occurring in highly disordered alloys due the compositional disorder as the one present in HEA. Such reasoning was already reported to explain high resistivity values in HEA thin films[80] and in Ni-based multicomponent alloys.[81] Assuming the classical approximation, a direct relation (Hagen–Rubens relation) between resistivity and emissivity can be accepted, so the mentioned large electron scattering can justify the relatively high emissivity observed in a broad wavelength range. Further studies, such as coupled resistivity and emissivity measurements, are

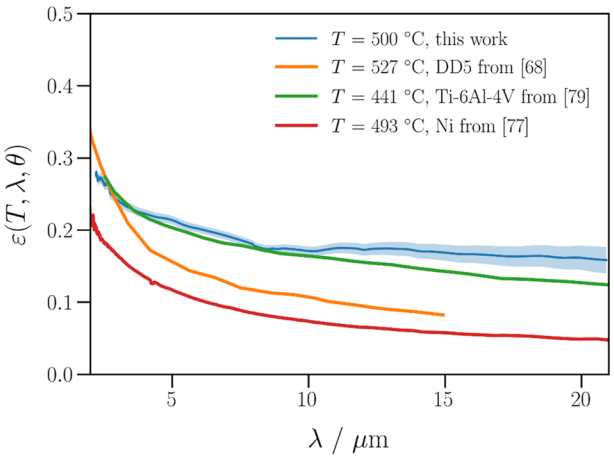

FIG. 16. Near-normal spectral directional emissivity with its expanded uncertainty (k = 2) at 500 °C compared to other data reported in the literature.

required to confirm if the validity of this explanation is fully correct, but at least it can be said that the high-entropy level of this type of alloys has a significant influence on the emissivity.

IV. CONCLUSIONS

The high-entropy alloy CrMnFeCoNi, consisting of 19.37 wt. % Cr, 18.92 wt. % Mn, 19.51 wt. % Fe, 20.77 wt. % Co, and 21.16 wt. % Ni, was prepared by the levitation melting of pure metals in vacuum. The microstructure of the alloy is composed mainly of a face-centered cubic (fcc) phase with a lattice parameter a = 0.3596 nm. The angle-dependent spectral directional emissivity was measured between 200 and 700 °C. Reproducible data were obtained upon several thermal cycles. The total directional emissivity is almost constant from 10° to 50°, and it increases up until it reaches a maximum around 70°. Integrating these data, the total hemispherical emissivity was determined, and it was observed that this property remains almost constant at 0.28 in a wide temperature range, showing a minor increase with increasing temperature. Spectral directional emissivity measurements allow us to detect incipient oxidation processes. These data show the necessity of measuring emissivity at working temperatures to achieve a precise quantification of radiative heat transfer.

AUTHOR DECLARATIONS

Conflict of Interest

The authors have no conflicts to disclose.

Author Contributions

Jon Gabirondo-López: Investigation (equal); Methodology (equal); Resources (equal); Validation (equal). **Iñaki López-Ferreño**: Investigation (equal); Methodology (equal); Validation (equal). **Boris Straumal**: Conceptualization (equal); Project administration (equal); Writing – review & editing (equal). **Alena Gornakova**: Formal analysis (equal); Investigation (equal); Software (equal); Validation (equal). **Anna Korneva**: Investigation (equal); Resources (equal); Visualization (equal); Writing – original draft (equal). **Olga Kogtenkova**: Formal analysis (equal); Project administration (equal); Resources (equal); Supervision (equal); Validation (equal). **Telmo Echániz**: Investigation (equal); Methodology (equal); Software (equal); Validation (equal). **Gabriel A. Lopez**: Conceptualization (equal); Validation (equal); Visualization (equal); Writing – original draft (equal); Writing – review & editing (equal).

DATA AVAILABILITY

The data that support the findings of this study are available within the article.

REFERENCES

[1] B. Cantor, I. T. H. Chang, P. Knight, and A. J. B. Vincent, "Microstructural development in equiatomic multicomponent alloys," Mater. Sci. Eng.: A **375–377**, 213–218 (2004).

[2] J. W. Yeh, S. K. Chen, S. J. Lin, J. Y. Gan, T. S. Chin, T. T. Shun, C. H. Tsau, and S. Y. Chang, "Nanostructured high-entropy alloys with multiple principal ele-

ments: Novel alloy design concepts and outcomes," Adv. Eng. Mater. **6**, 299 (2004).
[3]B. Pang, M. Wang, T. Liu, and X. Xi, "Effects of Al addition on tensile properties and aqueous corrosion behavior of Cantor alloy," J. Mater. Eng. Perform. **31**, 5602–5610 (2022).
[4]D. Wei, W. Gong, T. Tsuru, T. Kawasaki, S. Harjo, B. Cai, P. K. Liaw, and H. Kato, "Mechanical behaviors of equiatomic and near-equiatomic face-centered-cubic phase high-entropy alloys probed using *in situ* neutron diffraction," Int. J. Plast. **158**, 103417 (2022).
[5]K. A. Reunova, S. V. Astafurov, and E. G. Astafurova, "A temperature dependence of mechanical properties and fracture mechanisms in cast multiprincipal element alloys of the FeMnCrNiCo(N) system," Russ. Phys. J. **65**, 317–326 (2022).
[6]Z. Han, W. Ren, J. Yang, Y. Du, R. Wei, C. Zhang, Y. Chen, and G. Zhang, "The deformation behavior and strain rate sensitivity of ultra-fine grained CoNiFeCrMn high-entropy alloys at temperatures ranging from 77 K to 573 K," J. Alloys Compd. **791**, 962–970 (2019).
[7]T. Zhang, R. D. Zhao, F. F. Wu, S. B. Lin, S. S. Jiang, Y. J. Huang, S. H. Chen, and J. Eckert, "Transformation-enhanced strength and ductility in a FeCoCrNiMn dual phase high-entropy alloy," Mater. Sci. Eng.: A **780**, 139182 (2020).
[8]C. Haase and L. A. Barrales-Mora, "From high-manganese steels to advanced high-entropy alloys," Metals **9**, 726 (2019).
[9]J. Zhang, K. N. Yoon, M. S. Kim, H. S. Ahn, J. Y. Kim, Z. Li, T. Sasaki, K. Hono, and E. S. Park, "Strengthening by customizing microstructural complexity in nitrogen interstitial CoCrFeMnNi high-entropy alloys," J. Alloys Compd. **901**, 163483 (2022).
[10]E. G. Astafurova, E. V. Melnikov, K. A. Reunova, V. A. Moskvina, S. V. Astafurov, M. Yu. Panchenko, A. S. Mikhno, and I. Tumbusova, "Temperature dependence of mechanical properties and plastic flow behavior of cast multicomponent alloys $Fe_{20}Cr_{20}Mn_{20}Ni_{20}Co_{20-x}C_x$ (x = 0, 1, 3, 5)," Phys. Mesomech **24**, 674–683 (2021).
[11]P. Fan, N. K. Katiyar, X. Zhou, and S. Goel, "Uniaxial pulling and nano-scratching of a newly synthesized high entropy alloy," APL Mater. **10**, 111118 (2022).
[12]I. A. Alhafez, C. J. Ruestes, E. M. Bringa, and H. M. Urbassek, "Nanoindentation into a high-entropy alloy—An atomistic study," J. Alloys Compd. **803**, 618–624 (2019).
[13]T. Keil, D. Utt, E. Bruder, A. Stukowski, K. Albe, and K. Durst, "Solid solution hardening in CrMnFeCoNi-based high entropy alloy systems studied by a combinatorial approach," J. Mater. Res. **36**, 2558–2570 (2021).
[14]L. L. Xiao, Z. Q. Zheng, S. W. Guo, P. Huang, and F. Wang, "Ultra-strong nanostructured CrMnFeCoNi high entropy alloys," Mater. Des. **194**, 108895 (2020).
[15]Y. J. Li, A. Kostka, A. Savan, and A. Ludwig, "Atomic-scale investigation of fast oxidation kinetics of nanocrystalline CrMnFeCoNi thin films," J. Alloys Compd. **766**, 1080–1085 (2018).
[16]S. A. A. Shams, G. Jang, J. W. Won, J. W. Bae, H. Jin, H. S. Kim, and C. S. Lee, "Low-cycle fatigue properties of CoCrFeMnNi high-entropy alloy compared with its conventional counterparts," Mater. Sci. Eng.: A **792**, 139661 (2020).
[17]K. V. S. Thurston, B. Gludovatz, Q. Yu, G. Laplanche, E. P. George, and R. O. Ritchie, "Temperature and load-ratio dependent fatigue-crack growth in the CrMnFeCoNi high-entropy alloy," J. Alloys Compd. **794**, 525–533 (2019).
[18]M. Z. Ghomsheh, G. Khatibi, B. Weiss, M. Lederer, S. Schwarz, A. Steiger-Thirsfeld, M. A. Tikhonovsky, E. D. Tabachnikova, and E. Schafler, "High cycle fatigue deformation mechanisms of a single phase CrMnFeCoNi high entropy alloy," Mater. Sci. Eng.: A **777**, 139034 (2020).
[19]S. A. A. Shams, G. Kim, J. W. Won, J. N. Kim, H. S. Kim, and C. S. Lee, "Effect of grain size on the low-cycle fatigue behavior of carbon-containing high-entropy alloys," Mater. Sci. Eng.: A **810**, 140985 (2021).
[20]K. V. S. Thurston, B. Gludovatz, A. Hohenwarter, G. Laplanche, E. P. George, and R. O. Ritchie, "Effect of temperature on the fatigue-crack growth behavior of the high-entropy alloy CrMnFeCoNi," Intermetallics **88**, 65–72 (2017).
[21]K. S. Chung, P. M. Yiu, T. F. Hung, and C. H. Shek, "Strengthening and deformation mechanism of a $Fe_{20}Co_{20}Cr_{20}Mn_{20}Ni_{20}$ high entropy alloy with high nitrogen content," J. Alloys Compd. **871**, 159587 (2021).
[22]T. Stasiak, D. Oleszak, and A. Fraczkiewicz, "Effects of solidification conditions on microstructure and properties of high-entropy alloys from the CoCrFeMnNi family," JOM **74**, 4842–4852 (2022).
[23]A. V. Podolskiy, Y. O. Shapovalov, E. D. Tabachnikova, A. S. Tortika, M. A. Tikhonovsky, B. Joni, E. Ódor, T. Ungar, S. Maier, C. Rentenberger, M. J. Zehetbauer, and E. Schafler, "Anomalous evolution of strength and microstructure of high-entropy alloy CoCrFeNiMn after high-pressure torsion at 300 and 77 K," Adv. Eng. Mater. **22**, 1900752 (2020).
[24]T. Keil, E. Bruder, M. Laurent-Brocq, and K. Durst, "From diluted solid solutions to high entropy alloys: Saturation grain size and mechanical properties after high pressure torsion," Scr. Mater. **192**, 43–48 (2021).
[25]D. L. Foley, S. H. Huang, E. Anber, L. Shanahan, Y. Shen, A. C. Lang, C. M. Barr, D. Spearot, L. Lamberson, and M. L. Taheri, "Simultaneous twinning and microband formation under dynamic compression in a high entropy alloy with a complex energetic landscape," Acta Mater. **200**, 1–11 (2020).
[26]S.-P. Tsai, Y.-T. Tsai, Y.-W. Chen, P.-J. Chen, P.-H. Chiu, C.-Y. Chen, W.-S. Lee, J.-W. Yeh, and J.-R. Yang, "High-entropy CoCrFeMnNi alloy subjected to high-strain-rate compressive deformation," Mater. Charact. **147**, 193–198 (2019).
[27]Y. Xiao, R. Kozak, M. J. R. Haché, W. Steurer, R. Spolenak, J. M. Wheeler, and Y. Zou, "Micro-compression studies of face-centered cubic and body-centered cubic high-entropy alloys: Size-dependent strength, strain rate sensitivity, and activation volumes," Mater. Sci. Eng.: A **790**, 139429 (2020).
[28]A. Ehler, A. Dhiman, T. Dillard, R. Dingreville, E. Barrick, A. Kustas, and V. Tomar, "High-strain rate spall strength measurement for CoCrFeMnNi high-entropy alloy," Metals **12**, 1482 (2022).
[29]Y. Tang and D. Y. Li, "Dynamic response of high-entropy alloys to ballistic impact," Sci. Adv. **8**, 9096 (2022).
[30]Y. K. Kim, B. J. Lee, S.-K. Hong, and S. I. Hong, "Strengthening and fracture of deformation-processed dual fcc-phase CoCrFeCuNi and $CoCrFeCu_{1.71}Ni$ high entropy alloys," Mater. Sci. Eng.: A **781**, 139241 (2020).
[31]U. Glatzel, F. Schleifer, C. Gadelmeier, F. Krieg, M. Müller, M. Mosbacher, and R. Völkl, "Quantification of solid solution strengthening and internal stresses through creep testing of Ni-containing single crystals at 980 °C," Metals **11**, 1130 (2021).
[32]R. Gholizadeh, S. Yoshida, Y. Bai, S. Kurokawa, A. Shibata, and N. Tsuji, "Global understanding of deformation behavior in CoCrFeMnNi high entropy alloy under high-strain torsion deformation at a wide range of elevated temperatures," Acta Mater. **243**, 118514 (2023).
[33]A. Silvello, P. Cavaliere, S. Yin, R. Lupoi, I. Garcia Cano, and S. Dosta, "Microstructural, mechanical and wear behavior of HVOF and cold-sprayed high-entropy alloys (HEAs) coatings," J. Therm. Spray Tech. **31**, 1184–1206 (2022).
[34]A. Raturi, K. Biswas, and N. P. Gurao, "A mechanistic perspective on the kinetics of plastic deformation in FCC high entropy alloys: Effect of strain, strain rate and temperature," Scr. Mater. **197**, 113809 (2021).
[35]J. V. Gordon, R. E. Lim, M. J. Wilkin, D. C. Pagan, R. A. Lebensohn, and A. D. Rollett, "Evaluating the grain-scale deformation behavior of a single-phase FCC high entropy alloy using synchrotron high energy diffraction microscopy," Acta Mater. **215**, 117120 (2021).
[36]Z. Li, C. C. Tasan, K. G. Pradeep, and D. Raabe, "A TRIP-assisted dual-phase high-entropy alloy: Grain size and phase fraction effects on deformation behavior," Acta Mater. **131**, 323–335 (2017).
[37]S. Chen, H. S. Oh, B. Gludovatz, S. J. Kim, E. S. Park, Z. Zhang, R. O. Ritchie, and Q. Yu, "Real-time observations of TRIP-induced ultrahigh strain hardening in a dual-phase CrMnFeCoNi high-entropy alloy," Nat. Commun. **11**, 826 (2020).
[38]C.-L. Lin, J.-L. Lee, S.-M. Kuo, M.-Y. Li, L. Gan, H. Murakami, S. Mitani, S. Gorsse, and A.-C. Yeh, "Investigation on the thermal expansion behavior of FeCoNi and $Fe_{30}Co_{30}Ni_{30}Cr_{10-x}Mn_x$ high entropy alloys," Mater. Chem. Phys. **271**, 124907 (2021).
[39]D. Banik, S. Mandal, S. Mukherjee, H. Fujiwara, K. Ameyama, and K. Mondal, "The enhanced corrosion resistance of harmonic structured cantor alloy in Hank's simulated body fluid," J. Mater. Eng. Perf. **32**, 7965 (2023).
[40]J. Mahaffey, A. Vackel, S. Whetten, M. Melia, and A. B. Kustas, "Structure evolution and corrosion performance of CoCrFeMnNi high entropy alloy coatings produced via plasma spray and cold spray," J. Therm. Spray Tech. **31**, 1143–1154 (2022).

[41] T. Li, D. Wang, S. Zhang, and J. Wang, "Corrosion behavior of high entropy alloys and their application in the nuclear industry—An overview," Metals **13**, 363 (2023).
[42] B. Pang, M. Wang, Y. Shen, X. Xi, and Z. Niel, "Improvement in oxidation resistance of Cantor alloy through microstructure tailoring," China Foundry **19**, 503–510 (2022).
[43] P. Berthod, "Consequences of the additional presence of MC carbides on the behavior in oxidation at 1000 °C of a cast Cantor high entropy alloy," Mater. Corros. **74**, 1312–1323 (2023).
[44] M. L. Bürckner, L. Mengis, E. M. H. White, and M. C. Galetz, "Influence of copper and aluminum substitution on high-temperature oxidation of the FeCoCrNiMn 'Cantor' alloy," Mater. Corros. **74**, 79–90 (2023).
[45] Z. Zhang, D. E. J. Armstrong, and P. S. Grant, "The effects of irradiation on CrMnFeCoNi high-entropy alloy and its derivatives," Prog. Mater. Sci. **123**, 100807 (2022).
[46] T. Keil, E. Bruder, and K. Durst, "Exploring the compositional parameter space of high-entropy alloys using a diffusion couple approach," Mater. Des. **176**, 107816 (2019).
[47] H. Nam, C. Park, C. Kim, H. Kim, and N. Kang, "Effect of post weld heat treatment on weldability of high entropy alloy welds," Sci. Technol. Weld. Joining **23**, 420–427 (2018).
[48] T. A. Elmslie, J. Startt, S. Soto-Medina, Y. Yang, K. Feng, R. E. Baumbach, E. Zappala, G. D. Morris, B. A. Frandsen, M. W. Meisel, M. V. Manuel, R. Dingreville, and J. J. Hamlin, "Magnetic properties of equiatomic CrMnFeCoNi," Phys. Rev. B **106**, 014418 (2022).
[49] Ö. Özgün, D. Koch, A. Çakır, T. Tavşanoğlu, W. Donner, M. Farle, and M. Acet, "Magnetic properties of fcc and σ phases in equiatomic and off-equiatomic high-entropy Cantor alloys," Phys. Rev. B **106**, 214422 (2022).
[50] D. Billington, A. D. N. James, E. I. Harris-Lee, D. A. Lagos, D. O'Neill, N. Tsuda, K. Toyoki, Y. Kotani, T. Nakamura, H. Bei, S. Mu, G. D. Samolyuk, G. M. Stocks, J. A. Duffy, J. W. Taylor, S. R. Giblin, and S. B. Dugdale, "Bulk and element-specific magnetism of medium-entropy and high-entropy Cantor–Wu alloys," Phys. Rev. B **102**, 174405 (2020).
[51] J. Kamarád, M. Friák, J. Kaštil, O. Schneeweiss, M. Šob, and A. Dlouhý, "Effect of high pressure on magnetic properties of CrMnFeCoNi high entropy alloy," J. Magn. Magn. Mater. **487**, 165333 (2019).
[52] J. Šebesta, K. Carva, and D. Legut, "Role of magnetism in the stability of the high-entropy alloy CoCrFeMnNi and its derivatives," Phys. Rev. Mater. **3**, 124410 (2019).
[53] A. Smekhova, A. Kuzmin, K. Siemensmeyer, C. Luo, J. Taylor, S. Thakur, F. Radu, E. Weschke, A. G. Buzanich, B. Xiao, A. Savan, K. V. Yusenko, and A. Ludwig, "Local structure and magnetic properties of a nanocrystalline Mn-rich Cantor alloy thin film down to the atomic scale," Nano Res. **16**, 5626–5639 (2023).
[54] M. A. Al Hasan, J. Wang, S. Shin, D. A. Gilbert, P. K. Liaw, N. Tang, W. L. N. C. Liyanage, L. Santodonato, L. DeBeer-Schmitt, and N. P. Butch, "Effects of aluminum content on thermoelectric performance of Al CoCrFeNi high-entropy alloys," J. Alloys Compd. **883**, 160811 (2021).
[55] P. Pervan, V. M. Trontl, I. A. Figueroa, T. Valla, I. Pletikosić, and E. Babić, "Compositionally complex alloys: Some insights from photoemission spectroscopy," Materials **16**, 1486 (2023).
[56] Y. Yuan, Z. Xu, P. Han, Z. Dan, F. Qin, and H. Chang, "MnO_2-decorated metallic framework supercapacitors fabricated from duplex-phase $FeCrCoMnNiAl_{0.75}$ Cantor high entropy alloy precursors through selective phase dissolution," J. Alloys Compd. **870**, 159523 (2021).
[57] H. Kaypour, S. Nategh, R. Gholamipour, and A. Khodabandeh, "Effect of aluminum addition on microstructure, recrystallization and work hardening of MnCrCoFeNi high-entropy alloy," Trans. Indian Inst. Met. **76**, 119–133 (2023).
[58] J. Y. He, W. H. Liu, H. Wang, Y. Wu, X. J. Liu, T. G. Nieh, and Z. P. Liu, "Effects of Al addition on structural evolution and tensile properties of the FeCoNiCrMn high-entropy alloy system," Acta Mater. **62**, 105–113 (2014).
[59] J. Kumar, N. Kumar, S. Das, N. P. Gurao, and K. Biswas, "Effect of Al addition on the microstructural evolution of equiatomic CoCrFeMnNi alloy," Trans. Indian Inst. Met. **71**, 2749–2758 (2018).
[60] E. G. Campari, A. Casagrande, E. Colombini, M. L. Gualtieri, and P. Veronesi, "The effect of Zr addition on melting temperature, microstructure, recrystallization and mechanical properties of a cantor high entropy alloy," Materials **14**, 5994 (2021).
[61] S. Yamanaka, K. Ikeda, and S. Miura, "The effect of titanium and silicon addition on phase equilibrium and mechanical properties of CoCrFeMnNi-based high entropy alloy," J. Mater. Res. **36**, 2056–2070 (2021).
[62] N. Eißmann, U. Mühle, U. Gaitzsch, G. Walter, T. Weißgärber, and B. Kieback, "Precipitation hardening of high entropy alloy CoCrFeMnNi containing titanium," J. Alloys Compd. **857**, 157610 (2021).
[63] E. Babić, Đ. Drobac, I. A. Figueroa, M. Laurent-Brocq, Ž. Marohnić, V. M. Trontl, D. Pajić, L. Perrière, P. Pervan, G. Remenyi, R. Ristić, A. S. Fetić, D. Starešinić, and K. Zadro, "Transition from high-entropy to conventional alloys: Which are better?," Materials **14**, 5824 (2021).
[64] G. Bracq, M. Laurent-Brocq, C. Varvenne, L. Perriere, W. A. Curtin, J.-M. Joubert, and I. Guillot, "Combining experiments and modeling to explore the solid solution strengthening of high and medium entropy alloys," Acta Mater. **177**, 266–279 (2019).
[65] A. K. Chandan, K. Kishore, P. T. Hung, M. Ghosh, S. G. Chowdhury, M. Kawasaki, and J. Gubicza, "Effect of nickel addition on enhancing nanostructuring and suppressing TRIP effect in $Fe_{40}Mn_{40}Co_{10}Cr_{10}$ high entropy alloy during high-pressure torsion," Int. J. Plast. **150**, 103193 (2022).
[66] D. E. Jodi, J. Park, B. Straumal, and N. Park, "Investigation on the precipitate formation and behavior in nitrogen-containing equiatomic CoCrFeMnNi high-entropy alloy," Mater. Lett. **258**, 126806 (2020).
[67] U. Lee, B. Straumal, and N. Park, "Dynamic precipitation of σ-phase and element partitioning in equiatomic CoCrFeMnNi high-entropy alloy," Mater. Sci. Eng.: A **804**, 140739 (2021).
[68] B. Kong, T. Li, and Q. Eri, "Normal spectral emissivity measurement on five aeronautical alloys," J. Alloys Compd. **703**, 125–138 (2017).
[69] L. del Campo, R. B. Pérez-Sáez, L. González-Fernández, X. Esquisabel, I. Fernández, P. González-Martín, and M. J. Tello, "Emissivity measurements on aeronautical alloys," J. Alloys Compd. **489**, 482–487 (2010).
[70] T. Echániz, I. González de Arrieta, R. Fuente, I. Urcelay-Olabarria, J. M. Igartua, N. de La Pinta, W. Ran, H. Fu, J. Chen, P. F. Zheng, M. J. Tello, and G. A. López, "Thermal radiative properties of electron-beam-melted and mechanically alloyed V–4Cr–4Ti based alloys between 200 and 750 °C," J. Nucl. Mater. **513**, 86–93 (2019).
[71] D. Soler, P. X. Aristimuño, M. Saez-de-Buruaga, and P. J. Arrazola, "Determination of emissivity and temperature of tool rake face when cutting AISI 4140," Proc. Manuf. **41**, 304–311 (2019).
[72] M. Mazzarisi, A. Angelastro, M. Latte, T. Colucci, F. Palano, and S. L. Campanelli, "Thermal monitoring of laser metal deposition strategies using infrared thermography," J. Manuf. Processes **85**, 594–611 (2023).
[73] P. Michaleris, "Modeling metal deposition in heat transfer analyses of additive manufacturing processes," Finite Elem. Anal. Des. **86**, 51–60 (2014).
[74] J. Zhang, T. S. Fisher, P. Veeraraghavan Ramachandran, J. P. Gore, and I. Mudawar, "A review of heat transfer issues in hydrogen storage technologies," J. Heat Transfer **127**(12), 1391–1399 (2005).
[75] I. González de Arrieta, L. González-Fernández, E. Risueño, T. Echániz, and M. J. Tello, "Isothermal oxidation kinetics of nitrided Ti–6Al–4V studied by infrared emissivity," Corros. Sci. **173**, 108723 (2020).
[76] L. del Campo, R. B. Pérez-Sáez, X. Esquisabel, I. Fernández, and M. J. Tello, "New experimental device for infrared spectral directional emissivity measurements in a controlled environment," Rev. Sci. Instrum. **77**, 113111 (2006).
[77] I. González de Arrieta, T. Echániz, R. Fuente, J. M. Campillo-Robles, J. M. Igartua, and G. A. López, "Updated measurement method and uncertainty budget for direct emissivity measurements at the University of the Basque Country," Metrologia **57**, 045002 (2020).
[78] J. R. Howell, M. P. Mengüç, and R. Siegel, *Thermal Radiation Heat Transfer*, 5th ed. (CRC Press, Boca Raton, 2010).
[79] L. González-Fernández, E. Risueño, R. B. Pérez-Sáez, and M. J. Tello, "Infrared normal spectral emissivity of Ti–6Al–4V alloy in the 500–1150 K temperature range," J. Alloys Compd. **541**, 144–149 (2012).

[80]C. Wang, X. Li, Z. Li, Q. Wang, Y. Zheng, Y. Ma, L. Bi, Y. Zhang, X. Yuan, X. Zhang, C. Dong, and P. K. Liaw, "The resistivity–temperature behavior of $Al_xCoCrFeNi$ high-entropy alloy films," Thin Solid Films **700**, 137895 (2020).

[81]K. Jin, B. C. Sales, G. M. Stocks, G. D. Samolyuk, M. Daene, W. J. Weber, Y. Zhang, and H. Bei, "Tailoring the physical properties of Ni-based single-phase equiatomic alloys by modifying the chemical complexity," Sci. Rep. **6**, 20159 (2016).